

term by term, with the result<sup>38</sup>

$$W(\theta) = [1 + \frac{2}{3}\beta^{(2)} + (2/15)\beta^{(4)} + \dots]P_0(\cos \theta) + [\frac{1}{3}\beta^{(2)} + (2/21)\beta^{(4)} + \dots]P_2(\cos \theta) + [(1/35)\beta^{(4)} + \dots]P_4(\cos \theta) + \dots \quad (14)$$

In this expression

$$\beta^{(2k)} = \langle I^{2k} \rangle \langle l^{2k} \rangle / (2\sigma^2)^{2k},$$

where the averages over  $I^{2k}$  and  $l^{2k}$  are weighted by  $IT_I \exp(-I^2/2\sigma^2) / [\rho_c(I)\Gamma_I]$  and  $lT_l \exp(-l^2/2\sigma^2)$ ,

<sup>38</sup> E. C. Halbert (private communication).

respectively. In the first weighting factor,  $\rho_c(I)$  is the density, and  $\Gamma_I$  the decay width, of compound states with spin  $I$ .

A similar expansion with terms up to  $P_6(\cos \theta)$  has been published elsewhere.<sup>6</sup> However, two questionable approximations were made in obtaining the result. First, each of the  $\beta^{(2k)}$  was replaced by  $[\beta^{(2)}]^k$ . Second, the published formula includes only the first term of each square bracket in (14), thereby omitting terms of the same order as those it retains. If  $\beta^{(2)} \gg 1$ , the coefficients of  $P_4$  and  $P_6$  are small, but clearly one cannot now omit the term  $(\frac{2}{3})\beta^{(2)}$  in the coefficient of  $P_0$ . The  $\beta^{(4)}$  terms in the  $P_0$  and  $P_2$  coefficients may also be significant. It should be noted that  $\beta^{(2)}$  is likely to be of order unity whenever the anisotropy is easily visible.

### Electron Scattering by Calcium at 250 MeV\*

M. CROISSIAUX,† R. HOFSTADTER, A. E. WALKER, AND M. R. YEARIAN  
*Stanford University, Stanford, California*

AND

D. G. RAVENHALL‡  
*Università di Roma, Roma, Italy and University of Illinois, Urbana, Illinois*

AND

B. C. CLARK AND R. HERMAN  
*General Motors Corporation, Warren, Michigan*  
(Received 25 September 1964)

The doubly magic nucleus of Ca<sup>40</sup> has been investigated by the electron scattering technique at an incident energy of 250 MeV. The elastic scattering behavior has been resolved from the inelastic scattering, and absolute data on cross sections have been obtained for both types of events. In the case of the elastic scattering, the first and second diffraction features have been observed and measured. It has been possible to make a comparison of the elastic data with theoretical calculations based on a phase-shift analysis for certain assumed models of the nuclear charge density distribution. The combination of such an analysis with the present data, and also with earlier data on the same nucleus, permits the determination of the radius and skin thickness of the Ca<sup>40</sup> nucleus with a precision greater than has been attainable heretofore. An investigation of the dependence of the density distribution on a third parameter indicates that a Fermi distribution, or models close to this type, are required to fit the experimental data. A Fermi radial charge density distribution with radius  $c = 3.60$  F and skin thickness  $t = 2.50$  F fits the data extremely well.

#### I. INTRODUCTION

IT has been clear for some time that the behavior of the charge density in the ground states of many spherically symmetric nuclei of the periodic system can be reasonably well described by a distribution function approximately constant from the center of the nucleus ( $r=0$ ) to the neighborhood of the surface region where

the density gradually drops to the value zero. The distribution is characterized by the two parameters  $c$  and  $t$ , which represent, respectively, the distance to the half-density point and the 90%–10% “skin thickness.”<sup>1</sup> The evaluation of  $c$  and  $t$  is effectively related to the description of the charge density in the vicinity of the surface, and it is therefore the surface behavior that is best determined by the analyses of the previous published data. It is clearly desirable to know more about the behavior of the density function near the

\* This work was supported in part by the Office of Naval Research, and the U. S. National Science Foundation.

† Now at Centre de Recherches Nucléaires, Strasbourg-Cronenburg, France.

‡ On sabbatical leave from the University of Illinois, Urbana, Illinois during 1963–64.

<sup>1</sup> B. Hahn, D. G. Ravenhall, and R. Hofstadter, Phys. Rev. **101**, 1131 (1956).

center of the nucleus and also in the surface, particularly in the "tail" region where the density is very small. The so-called Fermi distribution<sup>1</sup> [see Eq. (1)] has given a satisfactory description of the charge density distribution in many nuclei. Recent theoretical work on a particular spherical nucleus, Ca<sup>40</sup>, has served to reinforce the value of distributions close to the Fermi model with perhaps a somewhat shorter tail, as a good choice for this nucleus.<sup>2,3</sup> In the work of Ravenhall, Herman, and Clark it was also shown that the muonic atom data are in satisfactory accord with a variety of shapes including the Fermi shape in Ca<sup>40</sup> with appropriate values of  $c$  and  $t$  lying in a relatively small range determined from electron scattering work.

Further progress in understanding the ground-state behavior of nuclei or nuclear matter involves learning more details about the density function. For example, it is desirable to determine a third parameter, in addition to  $c$  and  $t$ . This parameter could describe the central value of the charge density at  $r=0$ , or because of the normalization of the charge, the amount of charge in the tail, say, beyond  $r=c+t/2$ . Conceivably the Fermi model itself could turn out to be very successful and the specification of a third parameter might then fix on this model as particularly appropriate to actual nuclei.

The purpose of this paper is to face this question in the case of Ca<sup>40</sup>. In order to make progress with respect to previous investigations experiments have been carried out on Ca<sup>40</sup> at 250 MeV and we have been able for the first time to go beyond the second diffraction feature in the angular distribution of the differential cross section. These experiments and their analysis will be described in this paper. Further experiments at higher energies are also currently in progress and we hope to present additional information on the Ca<sup>40</sup> nucleus subsequently. Thus we look upon this paper as one of a series in which we shall continue to sharpen up, as much as possible, the description of the charge distribution in the spherical, doubly magic nucleus of Ca<sup>40</sup>. In working intensively on this previously studied nucleus we have felt that concentration on one definite nucleus can be very rewarding, not only because such a nucleus is representative of many other spherical and undistorted nuclei, but also because a comparison between electron scattering and muonic atom data can be made with a considerable degree of refinement. In this way the interaction of the muon with nuclear matter can be determined with high precision.

## II. EXPERIMENTAL METHODS

For the most part the apparatus used in obtaining the present results has been described previously.<sup>4-6</sup>

<sup>2</sup> D. G. Ravenhall, R. Herman, and B. Clark, *Phys. Rev.* **136**, B589 (1964).

<sup>3</sup> H. Crannell, R. Helm, H. Kendall, J. Oeser, and M. Yearian, *Phys. Rev.* **121**, 283 (1961).

<sup>4</sup> R. Hofstadter, F. A. Bumiller, B. R. Chambers, and M.

The special apparatus and conditions used in this experiment are as follows:

(1) The 72-in. spectrometer and ten-channel counter were used in all the work.

(2) The choice of incident energy was  $250 \pm 1.5$  MeV. The value of this energy depends on a recent calibration carried out by Janssens, Crannell, Parks, Rand, and Yearian using the floating-wire method. The width of the energy band employed was selected by the bunker slits between deflecting magnets in the energy-defining system and was 0.25%.

(3) The target material was made of naturally occurring samples of calcium metal. Since Ca<sup>40</sup> is present naturally to 96.97% and the remaining Ca isotopes are expected to scatter in a manner similar to Ca<sup>40</sup>, we do not make the small correction required for the presence of other calcium isotopes. On the other hand it is very difficult to avoid the presence of oxygen on the surface of the metal. The target was kept in silicone oil when not in use and was quickly transferred to the target chamber when placed in service where it was put under vacuum. Nevertheless the effects of a small oxygen impurity have been detected and have been allowed for (see below).

(4) For scattering angles less than 90°, the target angle was set so that the normal to the target bisected the angle between the beam and the angle at which the spectrometer was set. For scattering angles greater than 90° the supplementary angle was bisected by the normal to the target plane. The target was thin enough so that no correction is needed for the very small changes in solid angle caused by this resetting procedure at different scattering angles.

(5) Scattered electrons pass through the spectrometer and are detected in the ten-channel ladder.<sup>6</sup> The relative efficiencies of the different channels were measured as usual by using a carbon target to provide a flat inelastic continuum over the energy interval corresponding to the ten channels. The computer program of Crannell was used to correct for the channel efficiencies, radiative corrections, spectrometer dispersion, etc., and the data were then plotted automatically. As is usual with such measurements, four or five energy settings of the spectrometer are employed so that the peak appears in a different channel in each setting. The results are then combined by the computer program. In this way the effects of changing relative efficiencies can be averaged out. For example, Figs. 1 and 2 show the type of data obtained at 250 MeV and scattering

Croissiaux, *Proceedings of an International Conference on Instrumentation for High-Energy Physics, Berkeley, 1960* (Interscience Publishers, Inc., New York, 1961), pp. 310-315.

<sup>5</sup> H. Collard, R. Hofstadter, A. Johansson, R. Parks, M. Ryneveld, A. Walker, M. R. Yearian, R. B. Day, and R. T. Wagner, *Phys. Rev. Letters* **11**, 132 (1963).

<sup>6</sup> D. Aitken, R. Hofstadter, E. B. Hughes, T. Janssens, and M. R. Yearian, *Proceedings of the 1962 International Conference on High-Energy Physics at CERN*, edited by J. Prentki (CERN, Geneva, 1962), pp. 185-193.

angles of 43 and 55°, respectively. In these curves the full width at half-maximum is about 0.4%, as expected from the combination of various contributions to the resolution function. For example, the energy width of a single channel in the detector is about 0.35%.

In Fig. 2 the taller peak at the left corresponds to inelastic scattering from the lowest set of levels in  $\text{Ca}^{40}$ . The lowest  $\text{Ca}^{40}$  level is at 3.35 MeV above the ground state and thus is easily resolved from the  $\text{Ca}^{40}$  elastic peak. The lower remaining levels of  $\text{Ca}^{40}$  are too close to be resolved from each other by the spectrometer at

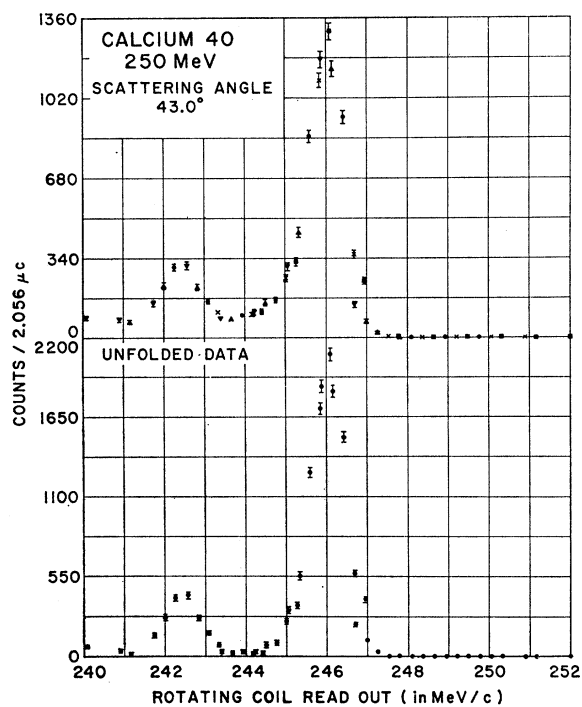


FIG. 1. Elastic and inelastic scattering peaks in  $\text{Ca}^{40}$  at 250 MeV. The scattering angle is 43°. The data plotted by the computer are shown when the data are not corrected as in (a) above, and when the data are corrected by the computer program of Crannell as in (b) below. The contributions due to the radiative tail associated with the peaks have been subtracted or "unfolded" in Crannell's program.

an incident energy of 250 MeV. The inelastic (level) scattering is larger at 55° than the elastic scattering peak because the elastic scattering is approximately at a minimum at 55° and 250 MeV. Under these conditions the presence of the oxygen impurity can be brought out, as indicated in Fig. 2.

(6) The elastic differential scattering cross-section values can be obtained in absolute units by comparing the scattering cross section from calcium with the cross section from hydrogen contained in a comparison polyethylene ( $\text{CH}_2$ ) target. The hydrogen cross sections were taken from well-established values at the low momentum transfer conditions of this experiment. Results are shown in Fig. 3.

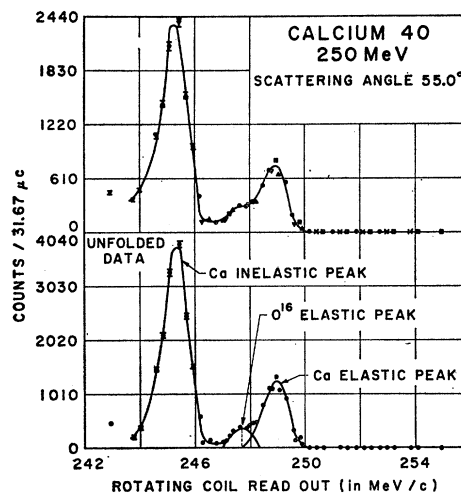


FIG. 2. This figure is similar to Fig. 1 except that the scattering angle is 55° and is near the first diffraction feature of calcium at an energy of 250 MeV. Under these conditions the small impurity of oxygen can be observed. (See text.)

(7) The presence of the contamination peak of  $\text{O}^{16}$  (see Fig. 2) permits a determination of the relative oxygen impurity to be made. The shift of the oxygen peak relative to the calcium peak arises from a recoil effect. In cases where recoil effects, at smaller angles, are insufficient to separate the oxygen and calcium peaks, the correction for oxygen impurity can easily be calculated. By using the data of Ehrenberg *et al.*<sup>7</sup> the oxygen cross section can be determined at various angles at 240 MeV. The slight adjustment of the cross section

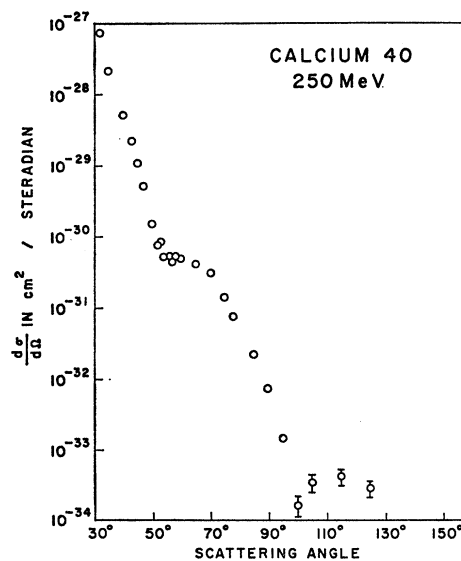


FIG. 3. This figure shows the differential elastic scattering cross section of calcium at 250 MeV. Where no statistical error is shown the error due to statistics is too small to be observed in the figure.

<sup>7</sup> H. F. Ehrenberg, R. Hofstadter, U. Meyer-Berkhout, D. G. Ravenhall, and S. E. Sobottka, *Phys. Rev.* **113**, 365 (1959).

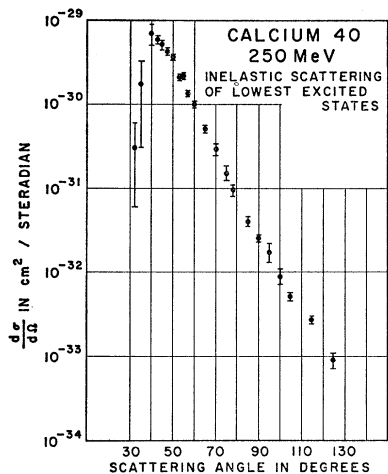


FIG. 4. The inelastic level scattering in calcium at 250 MeV. The figure shows the composite inelastic peak containing the four levels, 3.35, 3.73, 3.9, and 4.48 MeV, of which the middle two are probably the most important.

required by the conditions 55° and 250 MeV then allows us to calculate the relative oxygen-peak height at all other angles because of the calibration of absolute data made with the comparison hydrogen target. The contribution of oxygen to the calcium differential elastic cross-section peak could thus be obtained and was always less than 5%. The actual oxygen impurity amounted to about 3%.

### III. RESULTS

The results of our experiment are shown in Figs. 3 and 4 and in Tables I and II. The errors given are only statistical in nature. However, there are other causes of

TABLE I. Elastic electron scattering cross sections on calcium. Incident energy = 250 ± 1.5 MeV. Errors are statistical only. Angular resolution is 0.033 rad.

$\theta$ in degrees	Cross section in $\text{cm}^2/\text{sr}$
32	$7.48 \pm 0.41 \times 10^{-28}$
35	$2.18 \pm 0.12 \times 10^{-28}$
40	$5.16 \pm 0.18 \times 10^{-29}$
43	$2.30 \pm 0.09 \times 10^{-29}$
45	$1.16 \pm 0.04 \times 10^{-29}$
47	$5.09 \pm 0.20 \times 10^{-30}$
50	$1.62 \pm 0.07 \times 10^{-30}$
52	$7.85 \pm 0.78 \times 10^{-31}$
53	$8.22 \pm 0.40 \times 10^{-31}$
54	$5.46 \pm 0.55 \times 10^{-31}$
55	$5.46 \pm 0.30 \times 10^{-31}$
56	$5.42 \pm 0.33 \times 10^{-31}$
57	$4.37 \pm 0.19 \times 10^{-31}$
58	$5.46 \pm 0.40 \times 10^{-31}$
60	$4.97 \pm 0.19 \times 10^{-31}$
65	$4.28 \pm 0.22 \times 10^{-31}$
70	$3.07 \pm 0.13 \times 10^{-31}$
75	$1.55 \pm 0.07 \times 10^{-31}$
78	$7.76 \pm 0.40 \times 10^{-32}$
85	$2.26 \pm 0.13 \times 10^{-32}$
90	$7.46 \pm 0.30 \times 10^{-33}$
95	$1.66 \pm 0.21 \times 10^{-33}$
100	$1.70 \pm 0.57 \times 10^{-34}$
105	$3.58 \pm 0.60 \times 10^{-34}$
115	$4.44 \pm 1.00 \times 10^{-34}$
125	$2.93 \pm 0.80 \times 10^{-34}$

TABLE II. Inelastic electron scattering cross sections in calcium for the combined levels 3.35, 3.73, 3.9, 4.48 MeV. Incident energy = 250 MeV.

$\theta$ in degrees	Cross section in $\text{cm}^2/\text{sr}$
32	$\sim 0$
35	$17.6 \pm 17.00 \times 10^{-31}$
40	$70.00 \pm 20.00 \times 10^{-31}$
43	$58.66 \pm 8.40 \times 10^{-31}$
45	$52.97 \pm 5.30 \times 10^{-31}$
47	$43.21 \pm 2.70 \times 10^{-31}$
50	$37.00 \pm 1.60 \times 10^{-31}$
53	$21.15 \pm 0.80 \times 10^{-31}$
55	$23.42 \pm 0.80 \times 10^{-31}$
57	$13.16 \pm 0.36 \times 10^{-31}$
60	$10.00 \pm 0.35 \times 10^{-31}$
65	$5.17 \pm 0.36 \times 10^{-31}$
70	$2.92 \pm 0.30 \times 10^{-31}$
75	$1.49 \pm 0.15 \times 10^{-31}$
78	$9.65 \pm 1.00 \times 10^{-32}$
85	$4.02 \pm 0.50 \times 10^{-32}$
90	$2.58 \pm 0.02 \times 10^{-32}$
95	$1.86 \pm 0.40 \times 10^{-32}$
100	$8.80 \pm 4.00 \times 10^{-33}$
105	$5.14 \pm 0.35 \times 10^{-33}$
115	$2.75 \pm 0.27 \times 10^{-33}$
125	$8.94 \pm 2.00 \times 10^{-34}$

errors which are systematic and we can estimate them as follows:

- The target thickness is known only to within 2%.
- The entrance solid angle is known to about 1%.
- The Faraday cup efficiency might have been different for the calcium and hydrogen targets because of the varying amounts of multiple scattering under comparable experimental conditions. The Faraday cup was checked by the temporary use of a secondary emission monitor under a variety of conditions. In almost all cases it was found that the Faraday cup lost approximately 1.8% more integrated charge for calcium targets than for  $\text{CH}_2$  targets and this was allowed for in computing final cross sections. Simple theoretical calculations of multiple scattering are in agreement with this amount of relative loss of beam.

(d) In the forward angle region the cross section decreases by a factor of 1000 for an increase of 20° in the scattering angle. The cross section varies very rapidly therefore with the angle of scattering and amounts to approximately 4% for a change of 0.1°. Since the spectrometer setting in these experiments was known only to about 0.1° and the spectrometer entrance angle was 2° wide, the possible error due to the spectrometer setting is approximately  $\pm 4\%$  of the absolute cross section at forward angles.

(e) The cross section also varies very rapidly with incident energy. Simple calculations using the Born approximation (or the actual data we have previously obtained) show that a 1% change in incident energy produces a 10% change in the differential cross section of  $\text{Ca}^{40}$  near 40°. The effect is largest near 40°. Some of the larger variations in our experimental results are

probably due to an inability to set the energy to better than  $\pm 1.5$  MeV.

(f) The beam spot varies slightly in position on the target. The beam spot could be checked under most conditions, but at the smallest angles the beam intensity had to be reduced so that its image could sometimes not be clearly discerned. Hence the position of the beam spot could not be checked 100% of the time. For example, a shift of one quarter of an inch in the position of the beam spot could change the cross section by perhaps 15%. While such changes would be extraordinarily large we cannot exclude them at the very smallest angles.

Taken together, one can see that the various errors enumerated above could account for the type of spread observed in Fig. 3 which lies outside the statistical error.

In Fig. 4 we show the results obtained on the inelastic level scattering. Since there are four calcium levels very close to each other (3.35, 3.73, 3.9, 4.48 MeV) we could not resolve the separate peaks at an incident energy of 250 MeV. Because of the shape of the inelastic peaks we believe that the main contributions to the composite inelastic peak arise from the two levels at 3.7 MeV (3-) and 3.9 MeV (2+). The cross sections are given in Table II. A preliminary analysis shows that the angular distribution of these levels is consistent with a roughly even mixture of the (3-) and (2+) states.

#### IV. THEORETICAL ANALYSIS

The interpretation of the above results for the elastic process in terms of scattering by a static, spherically-symmetric charge distribution follows previous analyses in most features. As in Ref. 3, however, the absolute values of the measured cross sections now form an important additional part of the comparison between theory and experiment. The computational procedures have been given previously.<sup>2,8</sup> A new FORTRAN code written entirely in double precision arithmetic has furnished checks on the numerical results, which were largely obtained with the codes described previously. Thus we have confidence in the very small cross sections needed for comparison with the experiments.

The attitude we have adopted towards these new results is to re-examine the possible variations in charge distribution allowed by the earlier experiments at 183 MeV.<sup>1,2</sup> The main result of the earlier analyses was that "smoothed-uniform" charge distributions of a number of types were acceptable provided that the radius and skin thickness were chosen appropriately for each type. This was the same conclusion as had been drawn earlier for gold.<sup>1</sup> There was for calcium, however, an indication of a systematic variation in goodness of fit; the modified Gaussian shape gave a smaller  $\chi^2$  at

best fit than the Fermi shape and this in turn was better than the family II shape. The physically obnoxious trapezoidal shape was a further improvement. A possible conclusion was that the fit was sensitive to the amount of charge in the extreme tail of the charge distribution. An examination was also made at that time of the Fermi three-parameter shape, in which the Fermi function is multiplied by an expression quadratic in  $r$ , thus permitting a variation in charge density in the central regions. The unexpected result was obtained that the central density should be increased for a better fit, with a resulting negative tail to the charge distribution. There are reasons for believing that here, also, it was in fact the tail of the distribution which modifies the fit with experiment.

Similar results were obtained with the new data on scandium<sup>9</sup>: There was a tendency for shapes in which there was less charge in the tail to fit the experiments better. We reiterate that for each type of shape the radius and skin thickness are adjusted for a best fit, and then the best fits are compared. Results at a higher energy, or more specifically at larger values of  $q$  (the recoil momentum) were indicated: The diffraction structure at larger values of  $q$  would be expected to depend more sensitively on the details of the charge distribution.

The above results depended mainly on a fit to the relative cross-section measurements. It is clear that the use of absolute cross-section measurements allows considerable refinement in the parameter determination of any given charge distribution. The absolute cross-section comparison forms an important part of the present analysis.

The procedure adopted to follow the avenue suggested by the results at 183 MeV consists in examining the following shapes:

$$\rho_{c,z,n}(r) = \rho_1 \{ \exp[(r^n - c_1^n)/z_1^n] + 1 \}^{-1}. \quad (1)$$

This is a three-parameter shape which for  $n=1$  and  $n=2$  represents, respectively, the Fermi and modified Gaussian shapes. With  $c$  and  $z$  chosen to give the appropriate radius and skin thickness, the amount of charge beyond the 10% radius decreases as  $n$  increases, and (1) allows this to be done in a continuous way. The trapezoidal shape

$$\begin{aligned} \rho_{c,z}(r) &= \rho_2, & r \leq c_2 - z_2 \\ &= (\rho_2/2z_2)(c_2 + z_2 - r), & c_2 - z_2 < r \leq c_2 + z_2 \\ &= 0, & r > c_2 + z_2, \end{aligned} \quad (2)$$

is included as an extreme example of a short-tailed distribution. We have not considered further the family II shape. The possibility of a long tail, such as it possesses, is allowed here by making  $n$  less than 1 in (1).

<sup>8</sup> R. Herman, B. C. Clark, and D. G. Ravenhall, Phys. Rev. **132**, 414 (1963).

<sup>9</sup> The experimental work was carried out on scandium by F. Lewis, R. Hofstadter, A. E. Walker, Jr., and M. R. Yearian several years ago and has not been published. The analysis was carried out by Clark, Herman, and Ravenhall.

The Fermi three-parameter shape

$$\rho_{c,z,w}(r) = \rho_0 [1 + wr^2/c_3^2] \{ \exp[(r-c_3)/z_3] + 1 \}^{-1}, \quad (3)$$

although it has the unusual feature that  $\rho$  is negative for large  $r$  if  $w$  is negative, is included without modification. In Eqs. (1) and (2) the parameter  $z$  is related, respectively, to the 90–10% skin thickness as follows:

$$t \simeq 4.40 z_1^n / c_1^{n-1} n, \quad = 1.6 z_2.$$

However, values of  $t$  given in the tables are exact and have been obtained numerically.

Before describing the fitting procedure and results in detail, we can summarize our present conclusions: In both of the three-parameter shapes (1) and (3), the best fits turn out to be close to the Fermi distribution. The trapezoidal shape (2) is a very poor fit, and can be rejected. The narrowing down of possible shapes allowed in earlier analyses comes both from the new large-angle information and from the absolute cross-section values. Figure 5 for shapes (1) and (2) and Fig. 6 for shape (3) illustrate this result most clearly. The curves shown there are fits to the smaller angle data ( $\theta \leq 78^\circ$ ), with *no allowance* for absolute cross-section agreement. The agreement at the larger angles, and the extent to which each curve has been scaled to bring about the fit (see

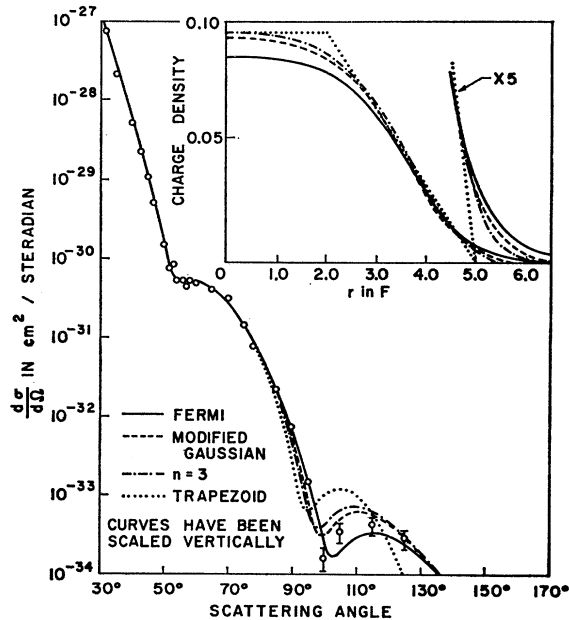


FIG. 5. Differential cross sections and charge distributions for shapes (1) and (2). Illustrated in this and the following figure are the best fits to the relative cross sections of the small-angle experimental points ( $\theta \leq 78^\circ$ ). Values of  $\chi^2$  are given in Table III, and parameter values are given in Table V. The theoretical curves have been scaled by the following factors to show the mutual agreement at the smaller angles:  $n=1$ , 1.16;  $n=2$ , 0.91;  $n=3$ , 0.84; trapezoid, 0.71. The deviations from experiment at larger angles are seen, and the scaling factors give the departure from experiment of the absolute value of the cross section, averaged over the small angle points. The best fits to all of the experimental points, with allowance for both relative and absolute values of the cross section, are shown in Figs. 7 and 8.

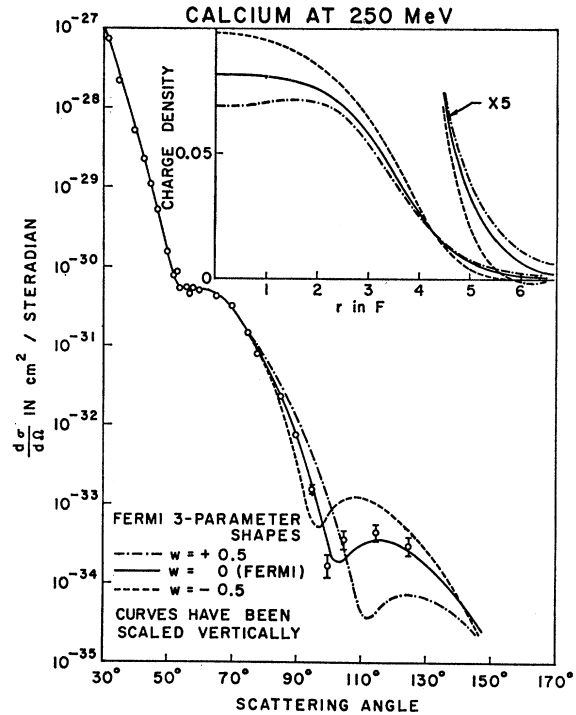


FIG. 6. Differential cross sections and charge distributions for shape (3). The curves illustrated are obtained in the manner described in the caption of Fig. 5. The scaling factors applied to them are as follows:  $w = +0.5$ , 1.61;  $w = 0$ , 1.16;  $w = -0.5$ , 0.72.

captions to figures) at the small angles, show how clearly the discrimination among these shapes can be made. The detailed procedure, including the finding of mutual best fits to both shape of the cross-section curve and absolute value, are described in the following section.

## V. FITTING PROCEDURE

As described in Sec. IIIC of Ref. 1 the cross section calculated on the assumption of potential scattering was folded over angles to simulate the angular resolution of the experiments. The parameter  $\Delta$  in the assumed Gaussian distribution was taken to be  $1^\circ$ . Nuclear recoil was disregarded at this stage. This has the slight computational simplification that cross sections need be calculated only at simple angular intervals. It has no effect on the comparison between different charge distributions, and the small effect on the absolute values obtained for  $c$  and  $z$  is estimated and included later.<sup>10</sup> The least-squares fitting procedure is designed

<sup>10</sup> Allowance for recoil may be estimated by examining the sensitivity of the calculated cross sections to small variations in  $c$  and  $z$ , in the region of the least-squares minimum. The effects produced by transforming the experimental cross section to the center-of-mass system can then be reproduced by changing  $c$  and  $z$  by the appropriate small amounts. In the work reported here there was a fortuitous cancellation between this effect and that of energy loss in the target. Consequently, to the accuracy of our present determination, zero correction is needed.

TABLE III. Results of least-squares fitting. The first two columns are from previous analyses of earlier data, and the rest are from the present work. The quantity  $\chi^2_{\text{rel}}$ , Eq. (4), is for a fit to the relative values of the cross section, with  $\lambda_{\text{min}}$  the scaling factor required, and  $\chi^2_{\text{tot}}$ , Eq. (5), is for a fit to both relative and absolute cross sections. In the third and fourth columns, a fit has been made to only the small angle data ( $\theta \leq 78^\circ$ ), to provide a comparison with the earlier analyses.  $E_\mu(2p \rightarrow 1s)$  is the energy of the muonic  $2p \rightarrow 1s$  x ray. The errors on the parameter values produce an uncertainty of about  $\pm 3$  keV in this quantity.

Column No.	1	2	3	4	5	6	7	8
	Calcium 183 MeV (Ref. 2)	Scandium 183 MeV <sup>b</sup>	Calcium 250 MeV small angles			Calcium 250 MeV all angles		
Shape	$\chi^2_{\text{rel}}$	$\chi^2_{\text{rel}}$	$\chi^2_{\text{rel}}$	$\lambda_{\text{min}}$	$\chi^2_{\text{rel}}$	$\lambda_{\text{min}}$	$\chi^2_{\text{tot}}$	$E_\mu(2p \rightarrow 1s)$ (keV)
(1) $n=1$ (Fermi)	9.0	59	23.6	0.87	28.9	0.88	31.3	782.4
(1) $n=2$ (modified Gaussian)	6.5	47	19.0	1.11	31.2	1.20	40.9	786.4
(1) $n=3$	...	...	18.2	1.20	42.6	1.32	64	787.7
(2) Trapezoid	4.5	...	17.7	1.43	88	1.90	385	792.4
(3) $w=+0.5$	12.8	136 <sup>a</sup>	35	0.63	96	0.58	134	776.5
(3) $w=0$ (Fermi)	9.0	...	23.6	0.87	28.9	0.88	31.3	782.4
(3) $w=-0.5$	4.3	...	17.2	1.39	76	1.64	179	794.3
(3) $w=-0.75$	4.2	...	...	...	...	...	...	...
Degrees of freedom	10	23	16		23		24	

<sup>a</sup> This scandium case corresponds to  $w = +1$ , but it is included here to show the trend of the results.  
<sup>b</sup> See Ref. 9.

to allow separately for the known statistical uncertainty in each angular measurement of the cross section, and for a possible over-all uncertainty in the absolute values. For fitting to the relative variation from one angle to another of the differential cross section, we calculate the quantity

$$\chi^2_{\text{rel}} = \sum_i [(\sigma_i - \lambda \epsilon_i) / \lambda \epsilon_i]^2 N_i / 2. \quad (4)$$

Here  $\sigma_i$  and  $\epsilon_i$  are theoretical and experimental values of the cross section at a particular angle, and  $N_i$  the number of counts, represents the statistical uncertainty in  $\epsilon_i$ . To allow for experimental uncertainties of non-statistical origin, the values of  $N_i$  inserted in (4) were limited by  $N_i \leq 150$ . The adjustable parameter  $\lambda$ , with respect to which (4) is minimized, represents the goodness of fit to the absolute measurement of the cross section. To incorporate its measure of the goodness of fit, we calculate the quantity

$$\chi^2_{\text{tot}} = \chi^2_{\text{rel}} + \mu(\lambda - 1)^2. \quad (5)$$

The number  $\mu$  expresses the relative weight given to the absolute cross-section measurement. In the results reported here, we use  $\mu = 500$ , so that a value of  $\lambda$  different from its measured value ( $=1$ ) by 10% adds 5 to  $\chi^2$ , i.e., it decreases the probability of a good fit by about a factor 3.

For each of the shapes described by (1), (2), and (3), and various values of the parameter  $n$  in (1) and  $w$  in (3), a mesh of values of  $c$  and  $z$ , the radius and skin thickness, were examined in the manner described, and minima in  $\chi^2$  obtained. The minimum values  $\chi_{\text{rel}}$  represent the goodness of fit to the experimental cross section ignoring its absolute value. The value of the adjustable parameter  $\lambda$  in (4) at minimum  $\lambda_{\text{min}}$  reveals how well such a fit also gives agreement with the experimental absolute values. The minimum values of  $\chi^2_{\text{tot}}$  represent a mutual best fit to both relative and absolute cross-section measurements. A list of values of  $\chi^2_{\text{rel}}$ ,  $\lambda_{\text{min}}$ , and

$\chi^2_{\text{tot}}$  is given in Table III, under the heading "250 MeV, all angles." Figures 7 and 8 show visually the differential cross sections for the best fits corresponding to  $\chi^2_{\text{tot}}$ , with inset graphs of the charge distributions.

The first two columns in Table III contain results of earlier analyses on calcium and scandium at 183 MeV. We note the results mentioned earlier that the shorter-tailed charge distributions [e.g.,  $n=2$  in (1), and,

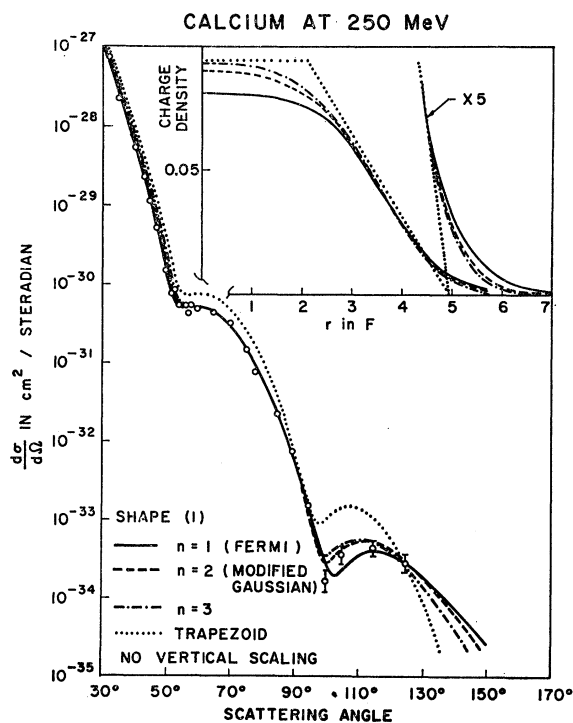


FIG. 7. Differential cross sections and charge distributions for shapes (1) and (2). The curves are best fits to both relative and absolute values of the experimental cross sections at all angles. Values of  $\chi^2$  are given in Table III, and parameter values in Table V. No vertical scaling has been applied.

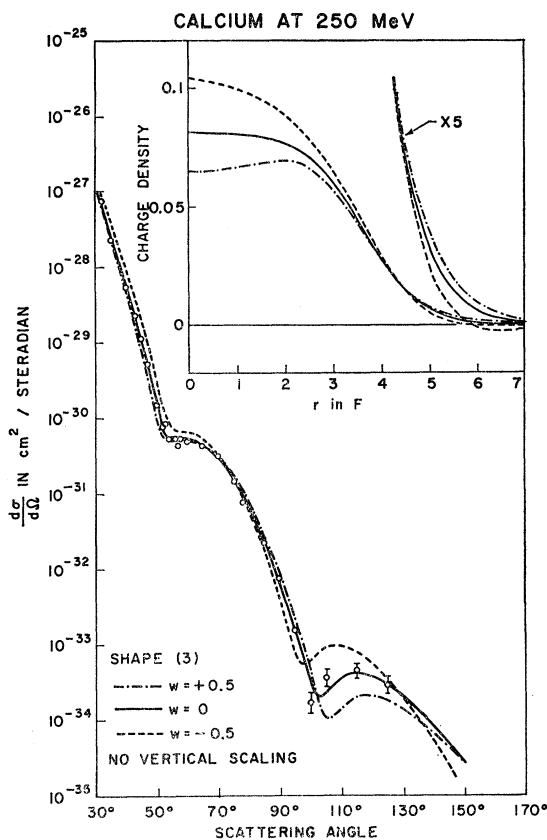


FIG. 8. Differential cross sections and charge distributions for shape (3). The curves are best fits as described in the caption to Fig. 7. No vertical scaling has been applied.

$w = -0.5, -0.75$  in (3)] were better fits to those relative cross-section measurements than the Fermi distribution ( $n=1$  and  $w=0$ ), while the longer tailed distribution ( $w = +0.5$ ) was a poorer fit. As a check on the consistency of the present 250-MeV data with those results (or alternatively as a test of the energy dependence of the whole procedure) we have also considered only those smaller angle points ( $\theta \leq 78^\circ$ ) which correspond in recoil momenta to the 183-MeV calcium data. The third and fourth columns list the values obtained for  $\chi^2_{\text{rel}}$  and  $\lambda_{\text{min}}$  in this case. The same tendency for shorter tailed shapes to give a better fit to the relative cross section is seen. The fit to the absolute cross section, i.e.,  $\lambda_{\text{min}}$ , becomes poorer, however, a feature which only the present measurements were capable of revealing. These results are presented graphically in Figs. 5 and 6, where the various best fits have been scaled vertically by  $1/\lambda_{\text{min}}$  to show their common behavior in the smaller angle region. Since in these graphs we have fitted only to the points at  $\theta \leq 78^\circ$ , the departures of the predictions at the larger angles are more pronounced than those of Figs. 7 and 8, where a mutual best fit to all of the data and to the absolute cross section, is made.

Having checked the consistency of our smaller angle

results with the earlier work, we look in detail at the fitting to the complete data, columns 5, 6, and 7 of Table III, and its graphical representation in Figs. 7 and 8. The three-parameter shapes (1) and (3) each have the Fermi distribution as a special case [ $n=1$  in (1), and  $w=0$  in (3)]. For each shape, the excursion of the third parameter from its Fermi value is now strongly limited. As previously noted, the trapezoidal shape (2) is a poor fit, and can be excluded. The fits to the relative cross section  $\chi^2_{\text{rel}}$  and to its absolute value,  $\lambda_{\text{min}}$  show the same tendency, which is an indication of the internal consistency of the experiments and our interpretation of them. As Figs. 7 and 8 show, the variation of each of the third parameters shifts the second diffraction maximum to larger or smaller angles compared with the Fermi shape, and at the same time decreases or increases the magnitude of the cross section in that region. The parameters  $c$  and  $z$  change in order to keep the first diffraction maximum in the same position. It is thus both the large-angle measurements, and the absolute cross-section determination, which gives us this new information about the charge distribution.

In column 8 of Table III we have also included the values these charge distributions predict<sup>11</sup> for the muonic x-ray transition energy  $E(2p \rightarrow 1s)$ . We have not at this stage attempted to combine the muonic x-ray measurements with our results. We note, however, that with the most recent experimental values for the energy,  $782.8 \pm 3$  keV according to the CERN-Darmstadt collaboration,<sup>12</sup> and  $780.7 \pm 0.8$  keV from a Chicago-Argonne collaboration,<sup>13</sup> the agreement with our final results (column 8) is best for shapes which fit the electron scattering cross sections best. In making comparisons, it should be remembered that the electron-scattering predictions of this energy are still uncertain by about  $\pm 3$  keV, owing to the error on our determination of the charge-distribution parameters. Measurements of the energy with this precision or better constitute valuable additional information in narrowing down the possible charge distributions.

The question of consistency among the various determinations of  $c$  and  $t$  for the Fermi shape is answered in Table IV. The values quoted contain more digits than are significant experimentally. The rows list results from the original analysis of the 183-MeV data,<sup>1</sup> a later examination of it<sup>2</sup> and the present work with the 250-MeV results. Included in the bottom row is a repetition of some of the work described here, with a somewhat larger estimate of the nonstatistical error present at each experimental point, i.e.,  $N \leq 75$ . There

<sup>11</sup> Our computational procedure for this calculation is sketched in Ref. 2, which also contains a comparison with previous electron-scattering and muonic x-ray results.

<sup>12</sup> D. Quitmann, R. Engfer, U. Hegel, P. Brix, G. Backenstoss, K. Goebel, and B. Stadler, Nucl. Phys. **51**, 609 (1964).

<sup>13</sup> S. Raboy (private communication). See also R. J. Powers, R. D. Ehrlich, J. A. Bjorkland, S. Raboy, and C. C. Trail, Bull. Am. Phys. Soc. **9**, 394 (1964). We thank Dr. S. Raboy for communicating this result to us.

TABLE IV. Values of  $c$ ,  $z$ , and  $t$  for the Fermi shape (1) with  $n=1$ , or (3) with  $w=0$  obtained from the least-squares analysis.  $c$  and  $z$  are the quantities occurring in (1) and (3), and  $t$  is the 90-10% skin thickness;  $R$  is the radius of the equivalent uniform model; they are given in F ( $10^{-13}$  cm). The first two rows come from earlier analyses, and the rest are from the present work. The rows labeled *small angles* are a fit to the relative cross sections for  $\theta \leq 78^\circ$ . The *all angles* rows are a fit to all of the points, one row for relative cross sections only, the other for both relative and absolute values. The corresponding  $\chi^2$  values are given in Table III. Errors on the 250-MeV parameters are estimated to be: on  $c$ , about 1%; on  $z$  and  $t$  about 5%.

Analysis	$c(F)$	$z(F)$	$t(F)$	$R(F)$
183 MeV				
HRH <sup>a</sup>	3.64	0.57	2.48	4.54
RHC <sup>b</sup>	3.64	0.56	2.44	4.51
250 MeV				
Small angles ( $N \leq 150$ )	3.576	0.598	2.61	4.59
All angles, relative ( $N \leq 150$ )	3.592	0.593	2.59	4.58
All angles, relative and absolute ( $N \leq 150$ )	3.602	0.576	2.51	4.54
Small angles ( $N \leq 75$ )	3.574	0.602	2.62	4.60

<sup>a</sup> Reference 1.

<sup>b</sup> Reference 2.

is only a very small change. The corrections needed for nuclear recoil and energy loss in the target cancel, so that zero net correction is needed. To illustrate the comparison, we plot in Fig. 9 the allowed values of  $c$  and  $z$  in the manner described in Ref. 2. The improved precision of our new analysis results in the smaller ellipses shown. The shaded band represents the CERN-Darmstadt value of the muonic x-ray energy ( $782.8 \pm 3$  keV).

The actual values of the parameters  $c$  and  $z$  at the best fit vary considerably among the shapes considered, although the end result is to give a charge distribution whose surface is pretty well determined, as is seen in Figs. 5, 6, 7, and 8 (insets). We list the numerical values obtained at the best fit in Table V for possible use by other workers. As with Table IV a recoil correction is

TABLE V. Values of  $c$ ,  $z$ , and related quantities, for the final best fit in each case, in F ( $10^{-13}$  cm). They all correspond to the row labeled *all angles, relative and absolute* in Table IV. Statistical errors on these quantities are:  $c$ , about 1%;  $t$ , around 5%. The corresponding differential cross sections are illustrated in Figs. 7 and 8. Interpolation between the various  $n$  values or  $w$  values is unreliable, because of the large step sizes.

Shape	$c$	$z$	$t$	$R$	$c/A^{1/3}$	$R/A^{1/3}$
(1) $n=1$ (Fermi)	3.602	0.576	2.51	4.54	1.05	1.33
(1) $n=2$ (modified Gaussian)	3.373	2.20	2.80	4.35	0.99	1.27
(1) $n=3$	2.384	3.22	2.73	4.29	0.70	1.25
(2) Trapezoid	3.510	1.419	2.35	4.08	1.02	1.19
(3) $w=+0.5$	3.307	0.600	...	4.79	0.97	1.40
(3) $w=-0.5$	4.105	0.612	...	3.96	1.20	1.16

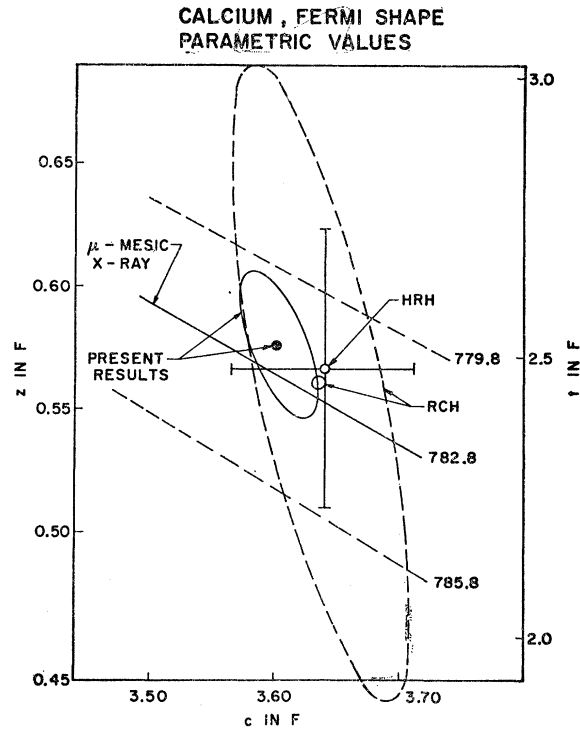


FIG. 9. Graphical representation of allowed parameter values for  $c$  and  $z$  for calcium from the least-squares fitting. The HRH (Ref. 1) value and the large ellipse from the RCH analysis (Ref. 2) are compared with the much more precise predictions now obtained. The muonic x-ray energy represented also on this plot is the CERN-Darmstadt result,  $782.8 \pm 3$  keV. A scale for  $t$  is given on the right.

included, and results are quoted to more digits than the accuracy of the determination warrants, since it is the comparison among the values that is useful.

To summarize, we now find, from two three-parameter studies, that distributions close to the Fermi distribution are indicated. To a good approximation, one may use a Fermi distribution with the parameter values

$$c = 3.60 \text{ F}, \quad t = 2.50 \text{ F}, \quad (z = 0.576 \text{ F}).$$

#### ACKNOWLEDGMENTS

We wish to thank the linear accelerator crew of the Stanford High Energy Physics Laboratory for providing the electron beam used in these experiments. One of us (M. C.) wishes to acknowledge the kind support of Professor S. Gorodetzky and the Centre National de la Recherche Scientifique (France) in sending him to work on this experiment at Stanford University.